# Three-dimensional characterization of fatigue cracks in Ti-6246 using X-ray tomography and electron backscatter diffraction

Soran Birosca, Jean-Yves Buffière, Francisco Alfredo García-Pastor, Mallikarjun Karadge, Laurent Babout, Michael Preuss

## To cite this version:

Soran Birosca, Jean-Yves Buffière, Francisco Alfredo García-Pastor, Mallikarjun Karadge, Laurent Babout, et al.. Three-dimensional characterization of fatigue cracks in Ti-6246 using X-ray tomography and electron backscatter diffraction. Acta Materialia, 2010, 58 (4), pp.1466. ⟨10.1016/j.actamat.2009.10.019⟩. ⟨hal-01822654⟩

**HAL Id: hal-01822654**
**https://hal.science/hal-01822654v1**

Submitted on 31 Jan 2023

# Three-dimensional characterization of fatigue cracks in Ti-6246 using X-ray tomography and electron backscatter diffraction

S. Birosca[a,*], J.Y. Buffiere[b], F.A. Garcia-Pastor[a], M. Karadge[a], L. Babout[c], M. Preuss[a]

[a]School of Materials, The University of Manchester, Manchester M1 7HS, UK
[b]Université de Lyon, INSA-Lyon, MATEIS UMR CNRS 5510, France
[c]Computer Engineering Department, Technical University of Łódź, Poland

In the present study, fatigue crack propagation was imaged non-destructively in three dimensions during in situ fatigue loading of Ti-6246 using X-ray microtomography on beam line ID19 at the European Synchrotron Radiation Facility. Phase contrast enabled the visualization of the two-phase microstructure and in combination with absorption contrast the crack chronology was recorded in situ during the fatigue experiment. In order to obtain the crystallographic orientation of individual grains along the crack path, a 3D electron backscatter diffraction volume was subsequently recorded. By combining both techniques it was possible to identify the role of prior β grain boundaries and the crystallographic orientation of the α lamellae on the crack path. It is shown that a near-surface crack that cuts across a prior β grain boundary is often diverted and crack bifurcation takes place. This results in local retardation of crack propagation and a first-order undulation of the crack front. In addition, the lamellar grain orientation and morphology causes a second-order crack front undulation with the tendency of large misorientations between α lamellae preferably orientated for prismatic $\langle a \rangle$ slip or pyramidal $\langle c + a \rangle$ slip deflecting the crack path.

*Keywords:* Titanium alloy; X-ray tomography; EBSD; Fatigue; Microstructure

## 1. Introduction

Two-phase $\alpha + \beta$ Ti alloys are widely used by the aerospace, power generation and biomedical industries because of their excellent mechanical and corrosion properties in addition to their relatively low density. Ti-6246 is a high-strength solid solution $\alpha + \beta$ Ti alloy used for relatively elevated temperature applications such as gas turbine compressors [1]. The exact temperature capability of Ti-6246 depends on the loading conditions during service. For long-term load-carrying applications the working temperature should not exceed 400 °C, while for short-term load-carrying applications the working temperature for Ti-6246 is up to 540 °C [2]. As in any other Ti alloy, the final microstructure is largely controlled by the thermomechanical processing route selected. For applications where damage tolerance is required, producing a fully lamellar microstructure enhances the fracture toughness [3,4], which is achieved by processing the material above the β-transus. In addition, the cooling rates applied at the end of such a process play a defining role in terms of lamellae width, colony size and shape. It is believed that the most influential microstructural parameter on the mechanical properties of a fully lamellar microstructure is the α colony size, because it determines the effective slip length [4]. For instance, applying high cooling rates results in a small colony size or eventually in a basket-weave structure, which increases the yield strength of the material [3–5].

In general, when Ti alloys are subjected to fatigue, the mechanical properties are strongly affected by the microstructure and the crystallographic texture of the material. It has been widely reported that fatigue crack initiation

---

[*] Corresponding author. Tel.: +44 7753165958.

*E-mail addresses:* soran.birosca@manchester.ac.uk, birosca73@hotmail.com (S. Birosca).

and growth is strongly influenced by the microstructure, grain size, grain orientation, grain boundary geometry, second phase precipitates and porosity [6]. Bin et al. reported that a coarse and inhomogeneous microstructure possesses a weak fatigue resistance [7]. Other studies showed that the colony microstructure in $\alpha + \beta$ Ti alloys exhibits the slowest crack growth rate, while the fastest rates are found in a fine-grained equiaxed microstructure [8,9]. Many of these aspects are related to the crystallographic anisotropy of the hexagonal close-packed (hcp) crystal structure of the $\alpha$ phase, with slip in the $\langle 11\text{–}20 \rangle$ direction ($\langle a \rangle$ slip) being significantly easier than slip in the $\langle 11\text{–}23 \rangle$ direction ($\langle c + a \rangle$ slip) [4]. In the case of fatigue properties, experimental studies showed that a fully transformed (lamellar $\alpha$) microstructure has a lower low-cycle fatigue resistance limit than an $\alpha + \beta$ annealed microstructure, with the fatigue properties of a bimodal (equiaxed $\alpha$ with transformed $\beta$) being superior to a purely equiaxed microstructure [3–5,10]. Thus, the fatigue properties are strongly affected by the microstructure.

In recent years, the initiation and short-crack behaviour at notches has been studied to a great extent [11–16] as foreign object damage and geometrical discontinuities in components can be responsible for fatigue crack initiation in aircraft structures. It is well known that notches within components can result in local stresses exceeding the yield strength of the material, resulting in plasticity. Under cyclic loading, this localized plasticity has the potential to cause initiation and subsequent propagation of fatigue cracks, leading to catastrophic failure of the component [11]. It has also been demonstrated that a short crack, at a given stress intensity factor, propagates faster than a long crack [12]. This difference between short and long cracks is usually explained by either: (i) the size of the short cracks being smaller than that of the controlling microstructural unit; (ii) the crack wake of a short crack being inadequate to produce crack closure [13]; or (iii) the size of the plastic zone being larger than the crack size for a short crack [14]. Thus, short crack initiation and propagation at the root of notches has received considerable attention in the literature [11–16].

The observation of a crack by conventional techniques such as optical or scanning electron microscopy (SEM) on a sample surface may be misleading particularly for short cracks as the microstructure has a significant effect on the three-dimensional (3D) crack shape. In order to study the micromechanics of short crack propagation, it is therefore crucial to characterize non-destructively short cracks in three dimensions, which requires the use of X-ray microtomography. Substantial improvements in synchrotron sources and detector technologies over the last decade mean that submicron spatial resolution is now readily available at specialized X-ray microtomography beam lines. In addition, the highly coherent beam at a synchrotron source provides phase contrast that increases the capacity to image low-contrast systems [17–19].

In the present study short crack propagation in a powder metallurgy processed Ti-6246 with a fully lamellar microstructure has been investigated by means of in situ fatigue testing using synchrotron X-ray microtomography combined with post-mortem 3D electron backscatter diffraction (EBSD) characterization. The possibility of high resolution in combination with phase contrast when using synchrotron X-ray microtomography allows one to study crack propagation non-destructively in three dimensions. In the case of Ti-6246 the phase contrast also enables one to visualize the Ti microstructure but without the crystallographic orientation information. This allowed detailed monitoring of the crack path, crack bifurcation and arrest, and relates these observations to the 3D microstructure, particularly prior $\beta$ grain boundaries. Additional EBSD mapping of slices from the studied volume provided the necessary crystallographic information of $\alpha$ lamellae along the crack plane in order to relate local crack propagation to crystallographic orientation. In the light of the new findings in the current study, the hypotheses and postulations with regards to fatigue crack propagation and microstructure correlations are critically reviewed.

## 2. Materials and methods

The alloy used in this study was a powder metallurgical (PM) processed Ti-6246 (Ti–6Al–2Sn–4Zr–6Mo), which was provided by Rolls-Royce plc in an as-hipped (hot isostatic pressed) condition. The reason for using PM-Ti-6246 in this work was the small $\beta$ grain size ($\sim$100 μm) in the as-received condition, which allowed control of the crack growth in the small samples necessary for the synchrotron X-ray microtomography experiment. Since the as-received material had a very fine lamellar microstructure, the material was first heat treated in argon atmosphere at 935 °C/2 h/water quenching and annealed at 875 °C/1 h/furnace cooling. The aim of this two-stage heat treatment was to generate a lamellar microstructure coarse enough to be revealed during the X-ray tomography experiment. The final microstructure is presented in Fig. 1a, which reveals that the $\beta$ grain size is still of the order of 100 μm and the $\alpha$ lamellae are arranged in basket-weave morphology. The average width of the $\alpha$ lamellae was 3–5 μm, which was considered to be sufficient to be resolved with the available resolution during the synchrotron X-ray tomography experiment. Due to the powder processing route, the material had a random crystallographic texture. Electrodischarge machining (EDM) was used to produce specimens for the in situ fatigue experiment with the geometry shown in Fig. 1b. In order to grow a crack in a defined position a triangular notch (2 μm wide, 100 μm long and 20 μm deep) was milled from the surface of the gauge centre using a focused ion beam (FIB) facility.

The X-ray microtomography experiment was carried out on beam line ID19 at the European Synchrotron Radiation Facility (ESRF), Grenoble, France. The experimental set-up

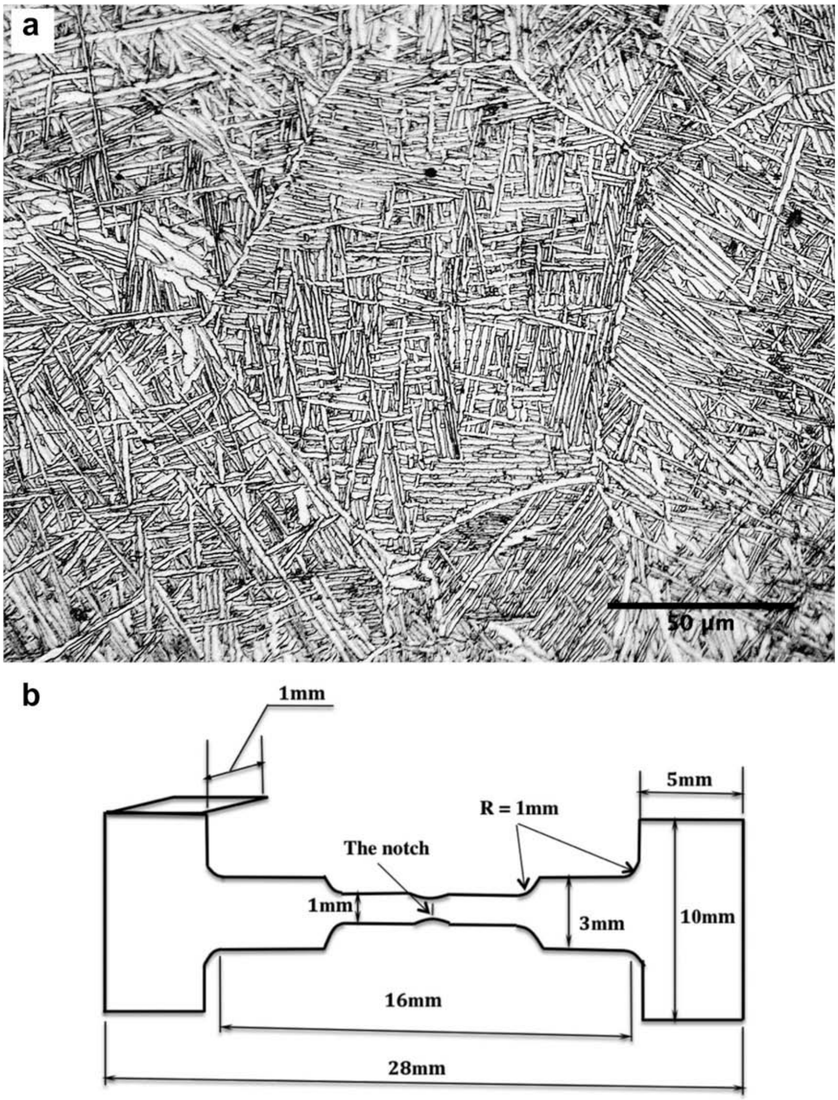

Fig. 1. (a) Optical micrograph of Ti-6246 after heat treatment showing fully lamellar microstructure. (b) Schematic representation of the fatigue specimen.

for such study is described in detail elsewhere [17,18]. The energy used during the experiment was 35 keV, which yielded sufficient X-ray transmission in the gauge section of the fatigue specimen. The voxel size was 0.7 μm with a 2048 × 2048 CCD-FReLoN (charge-coupled device–fast readout low noise) detector in order to analyze cross-sections with a maximum size of 1.4 mm and visualize the microstructure. The distance between the specimen and the detector was fixed at a distance of 200 mm in order to achieve sufficient phase contrast, which helps visualizing the two-phase microstructure. Tomographic imaging was carried out by interrupting the fatigue experiment after a certain number of cycles. An X-ray tomography scan comprised a set of 1500 radiographs, recorded over a 180° rotation around the vertical axis. It is important to note from a fatigue point of view that a scan took about 1 h while the sample was kept loaded at the maximum stress level since some titanium alloys show a deterioration of the fatigue properties under dwell fatigue conditions [20]. Each tomographic set was later reconstructed to a 3D volume using a 3D extension of a conventional 2D filtered back-projection algorithm.

The fatigue experiment was carried out in situ with a compact fatigue-testing machine set on the beamline rotating stage. An X-ray transparent polymethyl methacrylate tube was used to transmit the load between the lower mobile grip and the fixed upper grip. The fatigue test was a tension–tension experiment run with a frequency of 25 Hz, a maximum nominal stress of 460 MPa and a stress ratio of $R = 0.1$. The propagation of the fatigue cracks was checked by repeatedly cycling the samples ($N = 1000$ cycles) and taking a radiograph of the notched region. If a significant change in the radiographs was detected, a tomographic scan was recorded. This resulted in 13 tomographic scans being taken between 7000 and 27,000 fatigue cycles. The fatigue test was stopped before specimen failure in order to examine the sample by means of EBSD. The image quality of the tomogram was further improved by using a MATLAB code to remove ring artefacts developed by the ESRF staff based on ID19. The 3D data were visualized and analyzed using commercial image-processing software packages ImageJ and Amira. By measuring the crack dimensions from the tomograms it was possible to record the crack depth (*a*) to crack length (2*c*) throughout the experiment.

Following the analysis of the tomography data, areas of interest within the fatigued sample were identified for further EBSD studies. All EBSD scans were carried out using a Sirion field emission gun scanning electron microscope. The operating voltage used was 20 kV to optimize the quality of the diffraction patterns. The microscope is fitted with an HKL-EBSD system and the obtained data were analyzed using the Channel 5 software package. Subsequent EBSD scans were performed at 10, 30, 100, 150 and 250 μm below the sample surface by removing material (conventional grinding and polishing) along the ND direction, see Fig. 2. This quasi-3D construction of an EBSD map was necessary to identify the crystallographic information from individual α lamellae and β grains, which could not be obtained by X-ray microtomography. Since some aspects of the microstructure had already been recorded during the tomography study, it was possible to accurately align the EBSD maps with the tomograms and study, for instance, the impact of the crystallographic orientation of individual lamellae on local crack propagation.

## 3. Results and discussion

### *3.1. Crack aspect ratio and ΔK determination in three dimensions*

Fig. 3a–d shows selected 2D slices corresponding to the three principle planes around the crack (looking down the crack growth direction, LD–TD plane, Fig. 3a; crack plane from the top, ND–TD plane, Fig. 3b; crack from the side, ND–LD plane, Fig. 3c and d) taken from the tomogram after 27,000 cycles, where LD, TD and ND are loading, transverse and normal directions, respectively. From Fig. 3a and c it is possible to identify the prior β grain boundaries, which are occupied by grain boundary α. Fig. 3b shows a significant number of artefacts near the crack tip, which is a result of the high level of phase contrast [21]. The α lamellae microstructure is more difficult to identify and is only clearly revealed in some areas for specific grey-level and contrast settings. Consequently, in terms of microstructural description the tomograms were mainly used to identify the prior β grain boundaries. Fig. 3d shows the extent of the crack after 27,000 cycles near the deepest point of the crack, indicating that the crack has grown across three β grains.

The shape of a part through a crack can be described by an elliptical shape with an *a*/*c* ratio that can vary over a wide range from 0.1 to 1 [13,14,22]. For titanium alloys some authors have stated that a typical *a*/*c* ratio is 0.9 when studying long cracks [12]. The tomograms recorded during the in situ fatigue experiment enabled the visualization of the entire crack by first adjusting brightness and contrast levels of the 3D image to threshold the crack. In this way an isosurface of the crack shape was created that allowed crack depth and length to be determined throughout the fatigue experiment. Fig. 4a plots the crack length (*a* and *c*) as a function of fatigue cycle number (*N*) determined from the tomograms, while Fig. 4b displays the calculated *a*/*c* ratios from these measurements. It can be seen that the first X-ray tomography scan was carried out when the crack depth was around 50 μm, i.e. smaller than the average prior β grain size. and that the fatigue test was stopped when the crack had reached a depth of 200 μm and a length of about 300 μm. Consequently the crack had cut across about five β grains during the experiment. The fibbed notch had an *a*/*c* ratio of 0.4, and Fig. 4b shows that throughout the fatigue experiment the *a*/*c* ratio increased to a maxi-

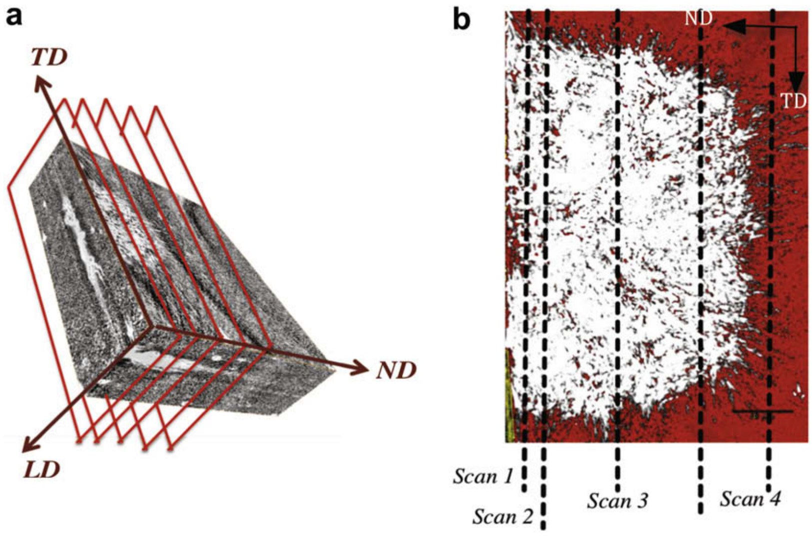

Fig. 2. Relating tomographed region to post-mortem EBSD scans (a), and highlighting exact scan positions with respect to the crack (b).

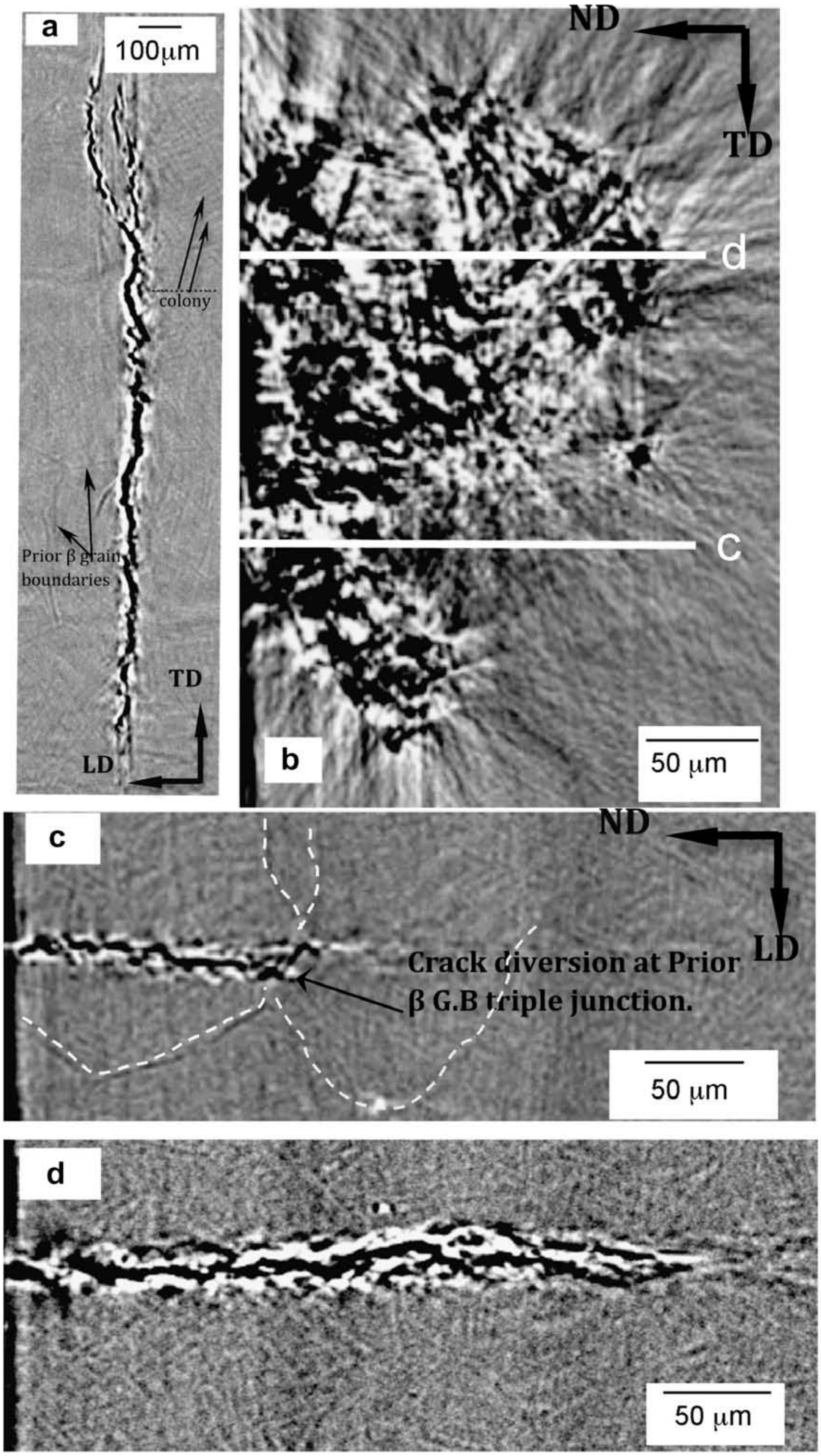

Fig. 3. 2D slices of the X-ray tomographs showing the crack after 27,000 fatigue cycles (LD–TD and ND–TD surface in a and b, respectively, and ND–LD surface in c and d).

mum value of about 1.2 without reaching a constant value after 27,000 cycles. Similar observations have been reported previously where for surface-breaking short cracks (100–500 μm) the *a*/*c* ratio increased from 0.1 to 0.7 [13], which was explained by the tendency of the crack driving force to restore an irregular crack front shape to a smooth one, i.e. $a/c = 0.7$ in this particular case. In order to understand the evolution of the crack shape, and the surprisingly high *a*/*c* ratio beyond 15,000 cycles, a 3D analysis of the stress intensity factor along the crack front and more detailed observations on the microstructural level were needed.

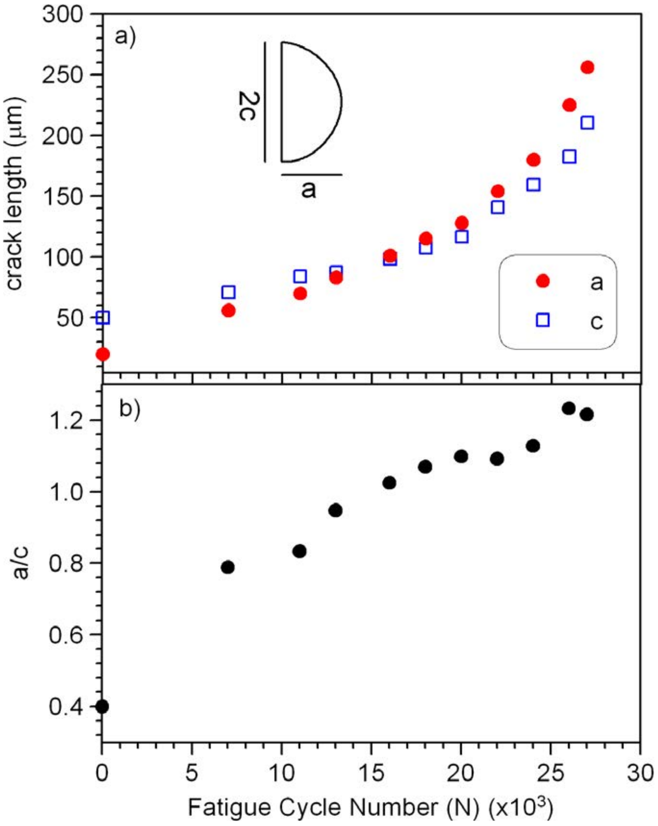

Fig. 4. Fatigue cycle number vs. (a) crack length and (b) $a/c$ ratio.

In order to understand 3D effects on crack propagation, the stress intensity factor range ($\Delta K$) was calculated in this study using Raju and Newmans's formulas [22]. More details about calculating the 3D $\Delta K$ values can be found in Refs. [14,23–25]. It is assumed that small-scale yielding conditions apply despite the physically short dimensions of the crack. In order to check the validity of this assumption for the present study, first the monotonic plastic zone size ($r_p$) of the crack was estimated using the following equation:

$$r_p = \frac{1}{\alpha\pi} \cdot \left(\frac{K_{\max}}{\sigma_y}\right)^2, \tag{1}$$

where $\alpha$ is a factor that depends on the plane stress–strain conditions prevailing at the crack tip ($\alpha = 2$ for plane stress and $\alpha = 3$ for plain strain) and $\sigma$ is the yield strength of the material (here estimated to be 1000 MPa). The second step was to determine the ratio of $r_p$ and the crack length at the surface ($r_{pc}/c$, assuming plane stress conditions) and in the bulk ($r_{pa}/a$, assuming plane strain conditions). Following this procedure, ratios of $0.1 < r_{pc}/c < 0.15$ (surface) and $0.031 < r_{pa}/a < 0.042$ (bulk) were calculated for the duration of the fatigue experiment. It is generally accepted that small-scale yielding conditions exist with $r_p/c$ values not exceeding 0.15 [24]. Consequently, it is reasonable to assume that small-scale yielding conditions prevail for the experimental conditions investigated here.

The 3D variation of the stress intensity factor range ($\Delta K$) along the crack front was then calculated using Raju and Newmans's formulas [22,25]. $\Delta K$ is calculated according to the following equation:

$$K_1 = \sigma\sqrt{\pi\frac{a}{Q}}F_S\left(\frac{a}{c}, \frac{a}{t}, \frac{c}{b}, \Phi\right), \tag{2}$$

where $\sigma$ is the applied stress, $Q$ and $F_S$ are geometrical factors, $t$ is the thickness of the sample, $b$ is the width of the sample and $\Phi$ is the angle between the sample surface and the normal of the crack front tangent.

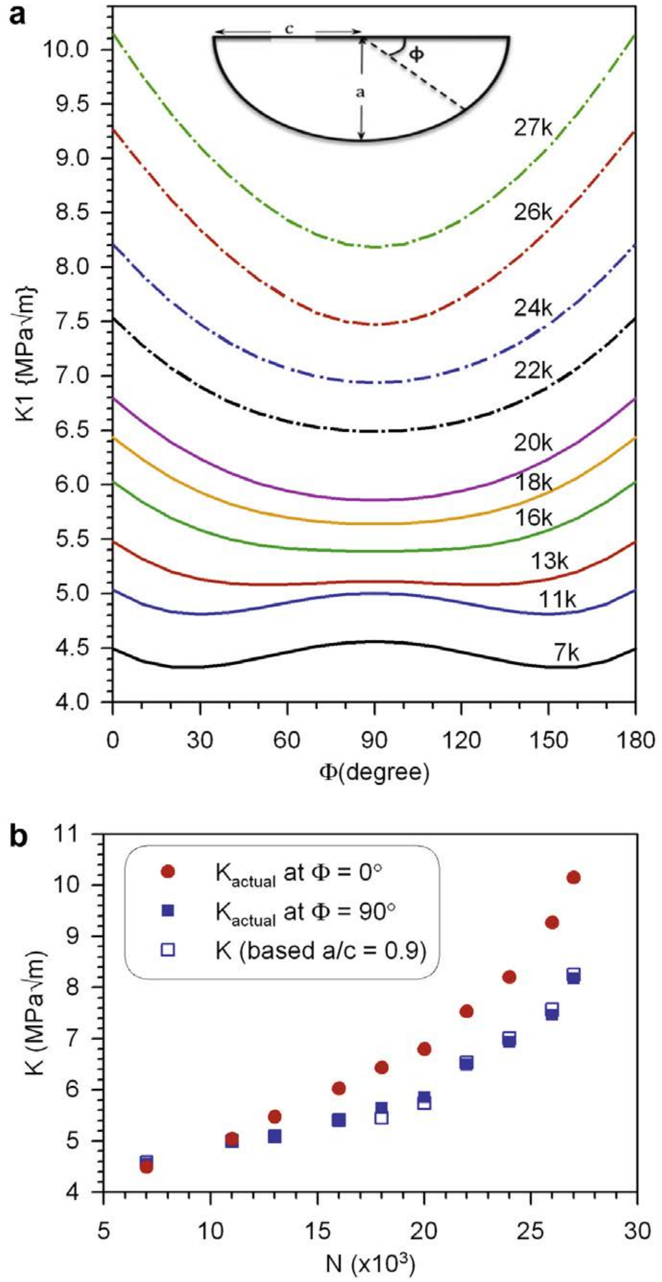

Fig. 5. (a) Maximum stress intensity factor calculations ($K$) considering the 3D crack shape effect according to Ref. [22] along the crack front at different fatigue cycle numbers, and (b) comparing $K$ values, using measured $K$ at $\Phi = 0°$ and 90° and calculated $K$ based on the theoretical value of $a/c = 0.9$.

The variation in the stress intensity factor along the crack front after different fatigue cycle numbers is shown in Fig. 5a. Note that the calculations were carried out assuming an ideal elliptical crack shape (shown in Figs. 5b and 6) with the experimentally measured $a/c$ ratios. The calculations show that during the early stage of the fatigue experiment ($N < 16{,}000$ cycles) only small variations (<10%) of the stress intensity factor along the crack front were observed, indicating that there should be little driving force to change the crack shape. As the crack continued to propagate, the calculated stress intensity factor increased faster near the surface ($\Phi = 0°$ and $180°$) compared to deep inside the material ($\Phi = 90°$), see Fig. 5b. Since the fatigue test was carried out under constant load, the stress intensity factor increased from an initial and nearly constant value of 4.5 MPa$\sqrt{\text{m}}$ to a final value of 8 MPa$\sqrt{\text{m}}$ for $\Phi = 90°$ and 10.2 MPa$\sqrt{\text{m}}$ for $\Phi = 0°$ and $180°$. Fig. 5b also displays the stress intensity factors calculated assuming a constant $a/c$ value of 0.9 [12] and using only the measurement of the crack length from the surface. The measurements confirm that even though the $a/c$ ratio varies between 0.8 and 1.25 for the observed short crack, the stress intensity factor calculation is hardly affected by this variation and the assumption of $a/c = 0.9$ provides accurate stress intensity values.

The calculations along the crack front as shown in Fig. 5a suggest that the crack should become increasingly shallow, which is opposite to what has been observed in Fig. 4b. Ferrie et al. postulated that such discrepancy is related to the variation in the plasticity-induced crack closure along the crack front [24]. Due to reduced constrain in the surface region, an increased level of plasticity can be expected in this region, resulting in increased levels of crack closure near the surface compared to the bulk region. Hence, the effective stress intensity factor might be smaller in the surface region compared to the bulk region, explaining the 3D shape of the observed crack. However, compared to the fine grain alloy studied by Ferrie et al. [24] for which plasticity was the dominant closure mechanism, the local microstructure of the studied alloy (and its interaction with the crack front) could also play an important role in driving the local crack shape. This point was investigated in detail and the results are presented below.

Fig. 6 visualizes the complete crack front evolution as recorded by X-ray tomography during the in situ fatigue experiment. When comparing the crack front after different cycle numbers to a perfectly elliptical shape, it is apparent that the crack front tends to deviate from the ideal elliptical shape, which will be referred to here as first-order undulation. In addition, a second-order undulation of smaller amplitude can be observed that seems to be more related to the α lamellar scale. In the case of the second-order undulation it is interesting to observe that some segments of the crack front which were slightly retarded at a given number of fatigue cycles had accelerated locally during the following fatigue cycles (see dashed rectangles). This effect has been discussed previously by Cox et al. [13,23]. They postulated that a crack front is highly irregular as some segments are blocked, for example, by grain boundaries, while other segments continue to propagate. Since a blocked segment becomes retarded relative to the rest of the crack, the stress intensity factor amplifies there. Once

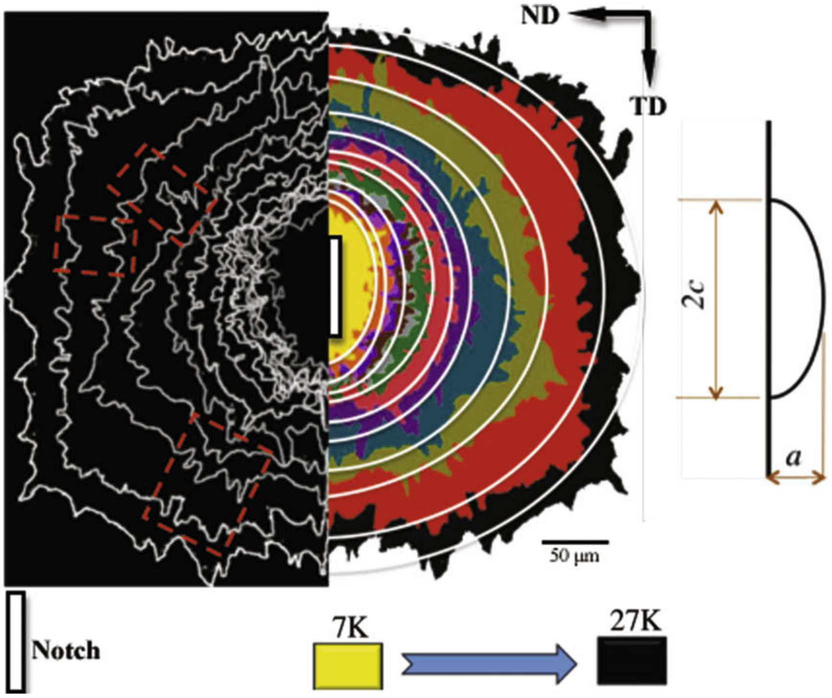

Fig. 6. Superimposed crack front images in different colors at various fatigue cycles (right), crack front edge thresholds (left) produced from the right mirror image.

the obstacle is overcome, the crack propagation in this area resumes at an “anomalously” rapid speed. The microstructural root cause for the observed second-order crack undulation and deviation are discussed in Section 3.3. The first-order crack undulation was found be to more related to crack shielding as discussed in the following section.

### *3.2. First-order crack undulation and prior β grain boundary correlation*

It is well established that the crack path and its propagation, as well as the crack front shape, can be strongly dependent on the loading axis direction, crystallographic orientation of the grains and original notch dimensions or shape [26–31]. Fig. 7 plots the individual crack shape in the ND–TD plane at different fatigue cycle numbers with the emphasis on visualizing the first-order undulation. It can be seen that the crack fronts do not propagate equally on the upper and lower sides. More specifically, between 10,000 and 22,000 cycles, the lower crack front side clearly propagates slower than the upper side as indicated by the arrows at 10,000, 18,000 and 22,000. Beyond 22,000 cycles, this trend is reversed. In order to understand this behaviour, the 3D crack is presented in Fig. 8 after 10,000 (Fig. 8a), 14,000 (Fig. 8b) and 26,000 (Fig. 8c) fatigue cycles, showing significant crack bifurcation (branching) in the lower part of the crack during the early stage of the fatigue experiment (Fig. 8a and b) and in the upper part of the crack near the end of the fatigue experiment (Fig. 8c). When analyzing all individual tomography scans, it became apparent that crack bifurcation was a dominant feature of the lower part of the crack between 7000 and 18,000 cycles and for the upper part of the crack after 22,000 cycles. Such crack bifurcation can be considered a crack-shielding mechanism, which decelerates the crack locally [30] and therefore explains the different crack propagation rates between the upper and lower part of the crack shown in Fig. 7.

The mechanism for crack bifurcation can be found in Fig. 9, which shows how the crack has interacted with the prior β grain boundary. It can be seen that whenever the crack has overcome a prior β grain boundary, it first gets diverted before a secondary crack forms. This secondary crack continues the main crack direction (mode I growth) and subsequently becomes the primary crack. As the identification of the prior β grain boundaries from the X-ray tomography data was not always completely unambiguous further analysis of the interaction of the crack with the prior β grain boundaries was carried out using EBSD. This technique allows one to discriminate β (body-centered cubic (bcc)) phase from α (hcp) phase as they have different crystal structures and lattice parameters [32,33]. The recognition of β phase in between α lamellar colonies assisted in determining the prior β grain size and shape. By plotting a β-phase inverse pole figure (IPF) map and superimposing it on the complete EBSD band contrast (BC) map, the prior β grain size and shape was clearly revealed—see Fig. 10a (scan 1 in Fig. 2b). In this figure, different colours represent β grains of particular crystallographic orientation, which are separated by thick black lines drawn for the purpose of visualization. In addition, schematic 3D cubes indicate the orientation of the β grains, and misorientation analysis showed that the high-angle boundaries between the β grains cut by the crack were at least 45°. Fig. 10a confirms that the crack diversions and bifurcations were in the vicinity of the prior β grain boundaries (see areas 1 and 2). Furthermore, it was of great interest to find the original point where the crack started to bifurcate (area 1). Therefore, the sample was polished further down from LD–TD surface along ND direction, as explained earlier, until the crack bifurcation point was reached. In Fig. 10b (scan 2 in Fig. 2b), it can be seen

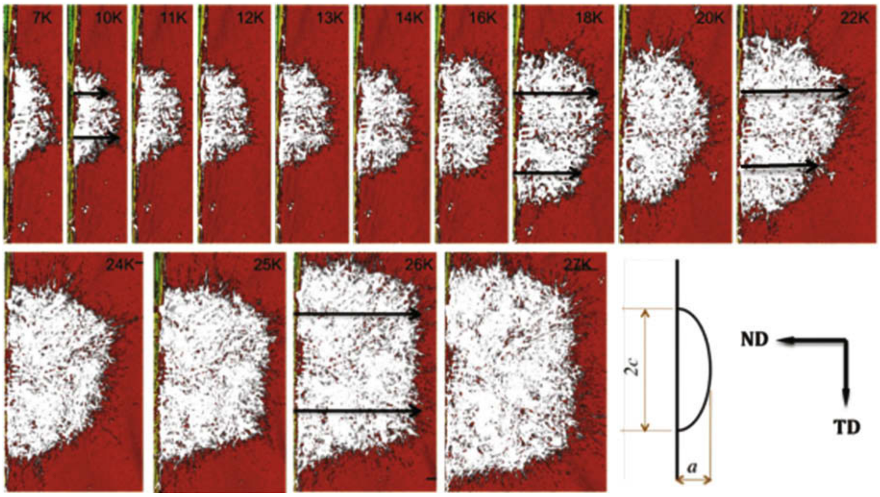

Fig. 7. 2D (TD–ND) crack front shape at different fatigue cycle numbers produced by ImageJ software. The crack front seems to propagate irregularly at the top and bottom sides of the crack.

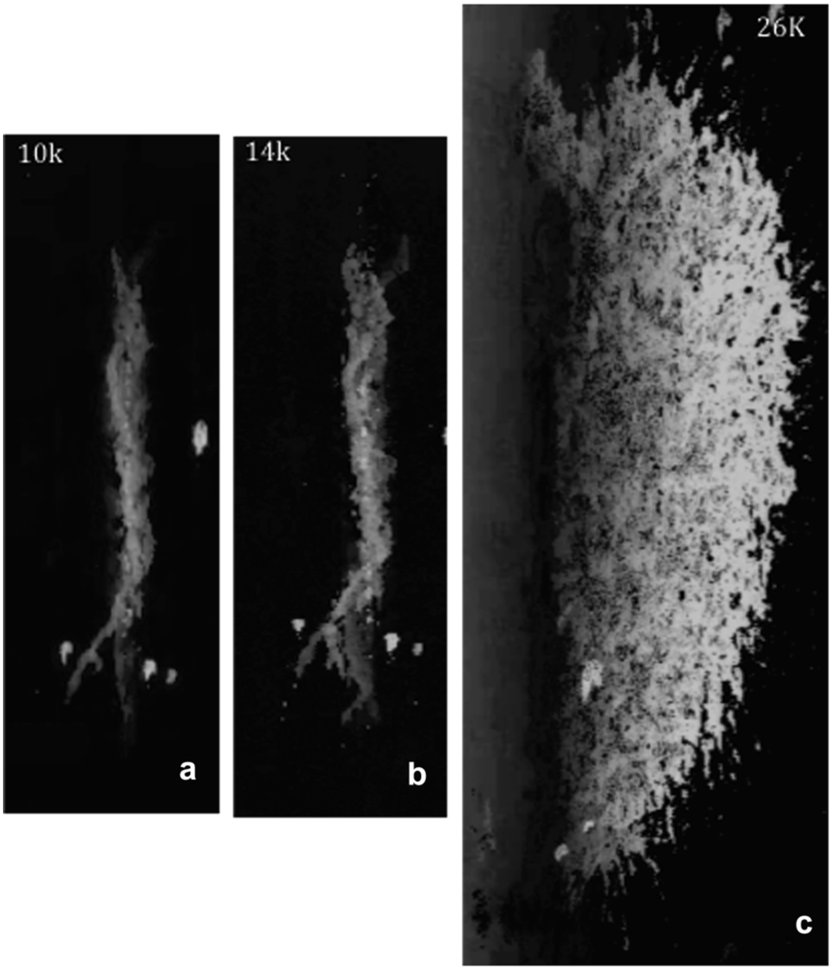

Fig. 8. Rotated 3D tomographs were taken at (a) 10,000, (b) 14,000 and (c) 26,000, showing crack bifurcation at both sides of the crack front.

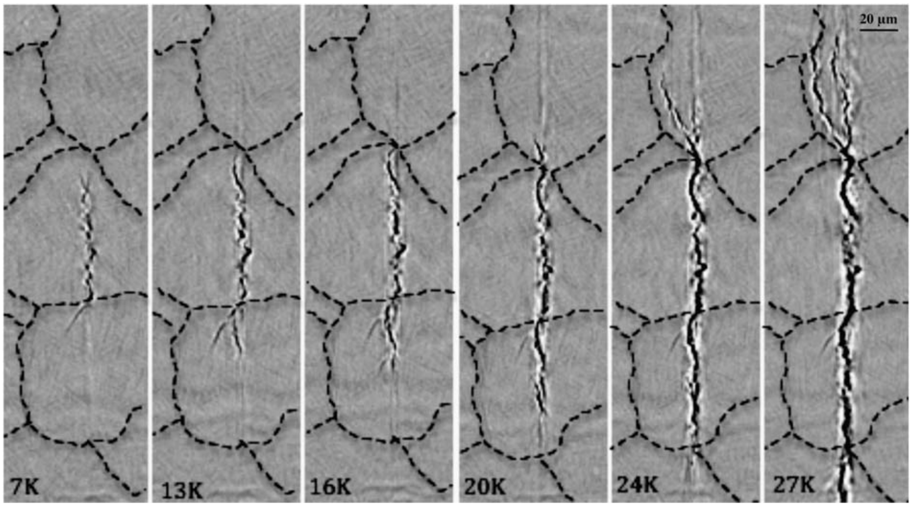

Fig. 9. Chronological description of interaction of the crack and prior β grain boundaries and triple junctions recorded by X-ray microtomography.

that both branches of the bifurcated crack are within one β grain. The steps of reaching the crack bifurcation point are shown in Fig. 10c (scan 3 in Fig. 2b) and Fig. 10d (scan 4 in Fig. 2b). In Fig. 10c, one of the branches shows clear discontinuities and has started to disappear, which indicates that the crack bifurcation point is very close. It is clear from Fig. 10d that the crack bifurcation has initiated at a prior β grain triple junction, where three or more β grains

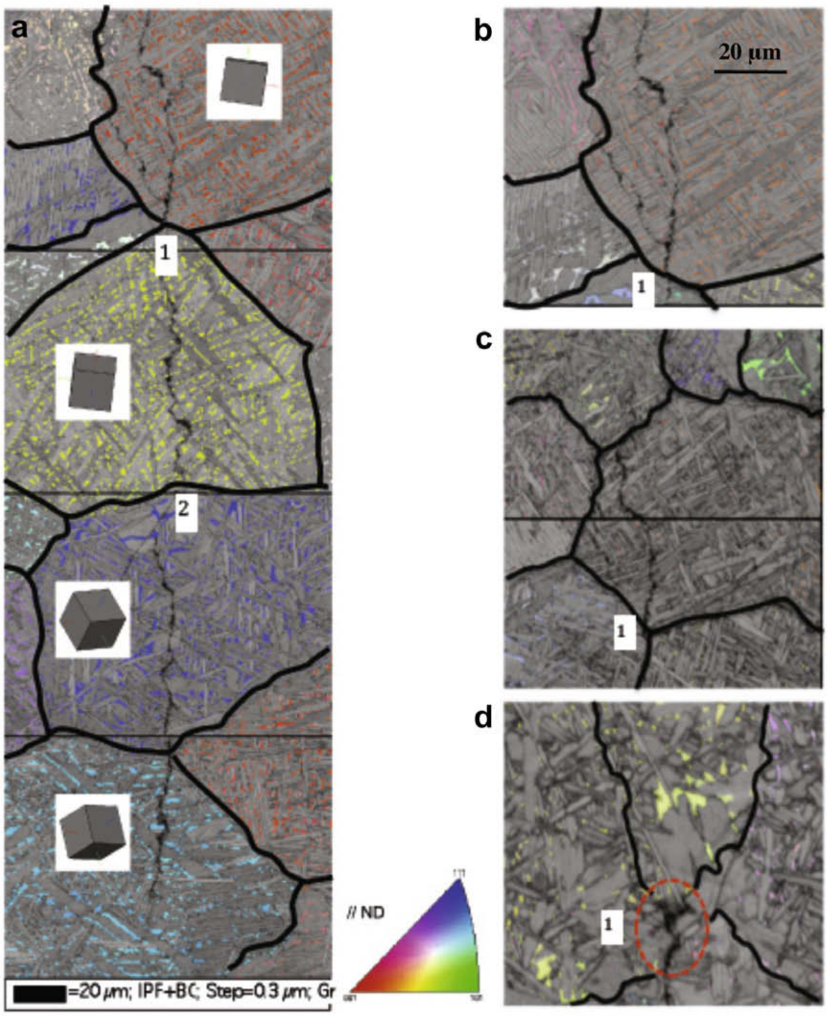

Fig. 10. (a) EBSD-derived IPF map of the β phase superimposed on a band contrast (BC) map in order to visualize grains and prior β grain boundary (scan 2). Same type of maps in (b–d) represent a 3D volume along the ND direction (b = scan 2, c = scan 3 and d = scan 4), visualizing the crack bifurcation at prior β triple junction.

with different crystallographic orientations meet. The EBSD observations were generally in excellent agreement with the X-ray tomography observations in terms of prior β grain boundaries and crack positions, confirming that these boundaries, particularly at triple points, play an important role in crack bifurcation and propagation.

Fig. 11 provides two different 3D views of the crack after 27,000 cycles, clearly demonstrating that crack bifurcation is only a feature observed near the surface but not deep inside the material, which explains why the *a*/*c* ratio becomes relatively large as the fatigue experiment proceeds. It seems that the high constraint in the bulk of the material prevents the prior β grain boundaries from becoming a source of crack bifurcation. At the same time, crack bifurcation near the surface, initiated by a deviation of the crack at the prior β grain boundary going into mode II growth, suggests increased ability of the material to shear near the surface.

In summary, X-ray tomography data have been used to understand the evolution of the *a*/*c* ratio and irregular crack front propagation (first-order undulation) and relate it to near-surface crack bifurcation. Crack bifurcation occurs when the crack enters a new β grain by first diverting the crack from mode I growth and subsequently forming a secondary crack that develops into a primary crack and continues to grow in mode I. The next step was to identify the root cause of the second-order undulation of the crack front, which required detailed microstructural analysis using EBSD, described in the following section.

### *3.3. Second-order crack undulation and α lamellar microstructure correlation*

In order to obtain an improved description of the lamellar microstructure along the crack path, secondary electron imaging and EBSD were carried out on the fatigued sample. As described earlier, the scans were carried out around the crack on the LD–TD plane at the surface of the fatigued sample as well as 10, 30, 100, 150 and 250 µm below the sample (LD–TD) surface (Fig. 2). The amount of mate-

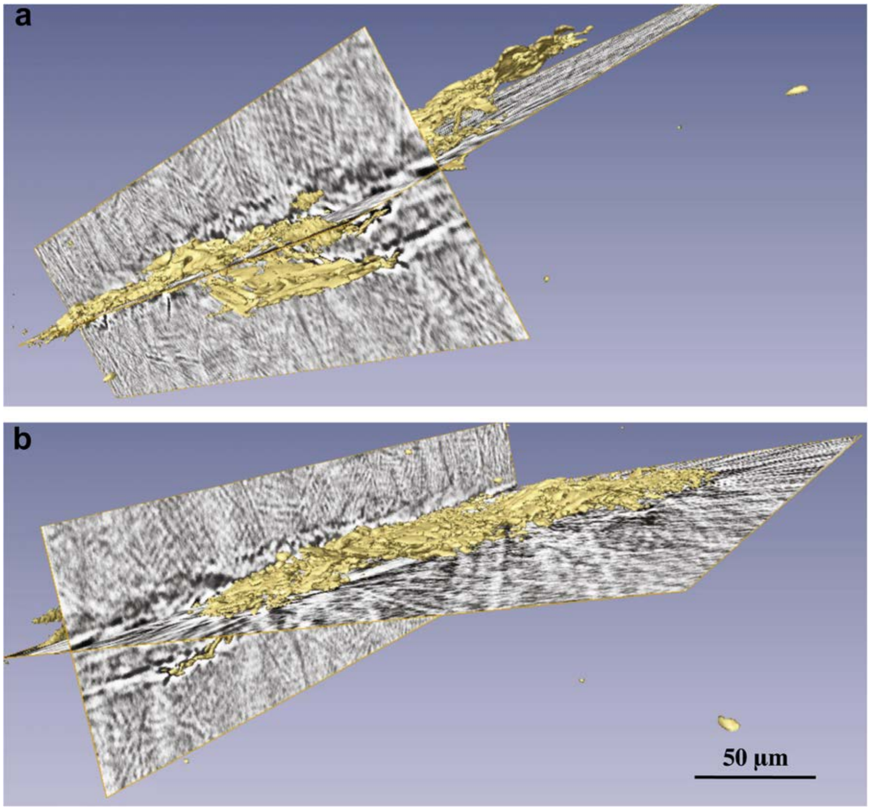

Fig. 11. Orthoslices showing microstructure in two dimensions with isosurface to highlight the crack in three dimensions at different viewing angles in (a and b), using Amira software.

rial removed between each EBSD scan was guided by the observation made during X-ray tomography. Particularly in the case of metals with an hcp crystal structure, transgranular fracture will be greatly affected by the crystallographic orientation of grains with respect to the applied stress axis due to the limited number of easy slip planes, whilst for intergranular failure the orientation of the boundary plane with respect to the stress axis and the misorientation between the grains are critical [32,34–36]. Fig. 12a provides a typical overview of crack/microstructure interaction recorded by an EBSD-derived BC map at 10 µm below the surface (scan 1 in Fig. 2b). In general, all EBSD maps (scans 1–5, Fig. 2b) revealed that the majority of the crack propagation is of translamellar nature with only few segments of the crack having grown parallel to the lamellar interface (referred to as interlamellar).

Secondary electron SEM images in Fig. 12b and c show the effect of the lamellar grain boundary geometry on the crack path across the lamellar structure. As can be seen from these figures, in most cases the crack crosses the lamellar colonies at a 90° angle to one in-plane direction of the $\alpha/\beta$ interface. Therefore, even though macroscopically the crack appears to be a mode I crack as usually reported in the literature [6,27,28,35,37,38], microscopically it seems to be more a mode II or mixed-mode crack interacting closely with the lamellar microstructure. Bache and Evans [27] also found that the $\alpha$ colony morphology affects the crack growth direction. However, they did not observe that the crack tends to cross lamellae where the interface boundary is close to 90°. Hu et al. [6] reported that cracking can occur close to 90° to the interface boundary, but also argued that interlamellar cracking can occur at a random angle between the $\alpha/\beta$ boundary trace and the loading direction, even at an angle as small at 10°. Their findings suggest that apart from the applied stress, the internal stresses within individual colonies resulting from the elastic anisotropy and constraint during loading can play a significant effect on the interlamellar crack growth. For short crack propagation, Hu et al. found that one of the favourable conditions for a short crack to propagate into the next grain/colony is that the microstructure allows the angle between the microcrack and the loading axis to be close to 90° [6]. Overall, there is uncertainty in correlating grain/lamellar boundary morphology and orientation to crack propagation although it seems to be clear that in two-phase titanium alloys the microstructure plays an important role in affecting the crack path. Work by Bhattacharyya et al. [1] has demonstrated that lamellar colonies, which appear to have very different orientations when simply studied optically, might in fact have identical or at least very similar crystallographic orientations. Consequently, it is important to identify the exact crystallographic orientation of the lamellae along the crack path and relate these to the loading direction. In addition, the

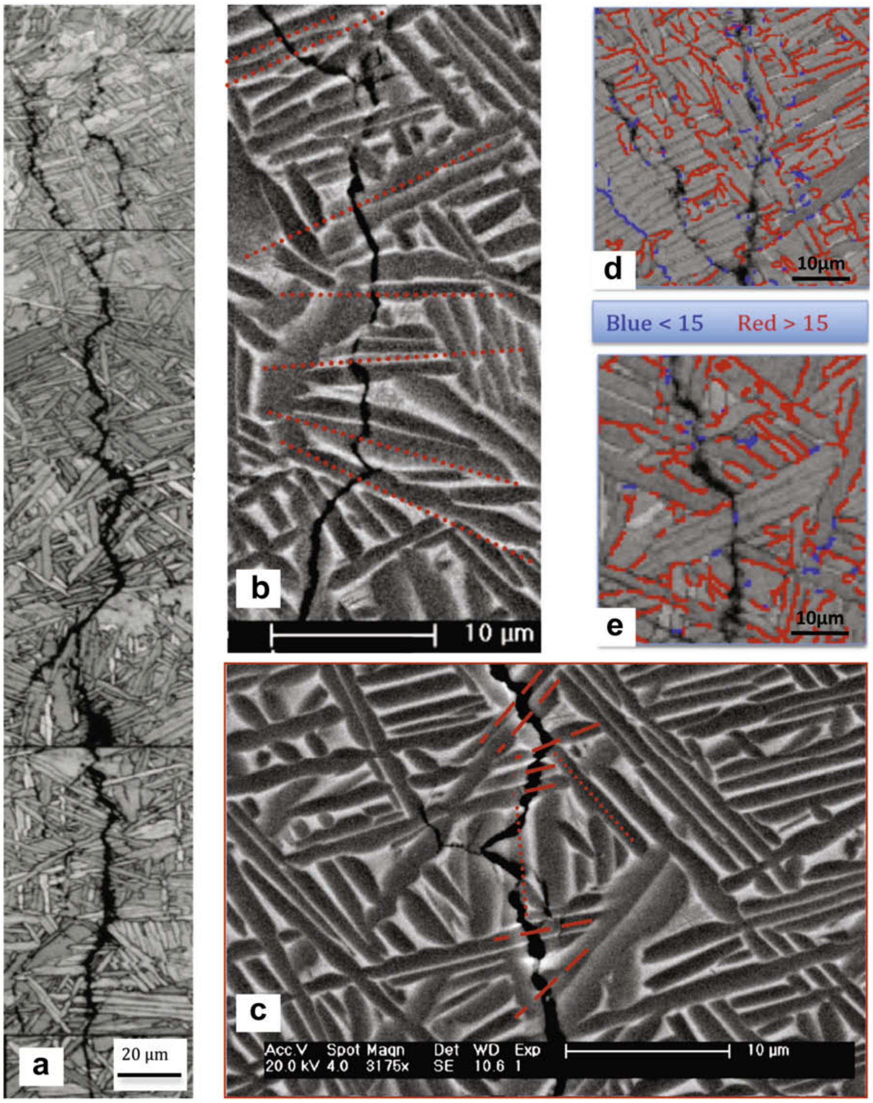

Fig. 12. (a) EBSD-derived band contrast map. (b and c) SEM images showing the effect of grain boundary geometry on the crack path across the lamellar structure. (d and e) EBSD-derived grain boundary level maps showing the effect of grain boundary characteristics on the crack path.

crack growth might also be determined by grain boundary misorientation, which again requires detailed studies on the microstructural scale using EBSD as described in the following paragraphs.

It is universally accepted that the grain boundary geometry plays an important role in crack nucleation and propagation [6,7,32,35,36]. For instance, high-angle grain boundary or slip bands in the vicinity of the grain boundary are favourable locations for crack nucleation, or in other words, high-angle boundaries are always more sensitive to cracking than low-angle boundaries. On the other hand, the likelihood is higher for a crack to be arrested by a high-angle boundary rather than a low-angle grain boundary as the grain boundary acts as a strong obstacle to short crack growth [32,36]. The effect of misorientation between α lamellae on the crack path is shown in Fig. 12d and e. As indicated in both maps, the red grain boundaries display greater than 15° misorientation between α lamellae, whereas the blue grain boundaries indicate misorientation between α lamellae in the range of 2–15° (see online version). The lamellar boundaries that are only recognized from the underlying band contrast map are those having less than 2° misorientation, i.e. boundaries within a lamellar colony. As can be seen from this figure, straight crack paths within lamellar colonies (<2° misorientation) are observed, while the crack changes its direction when confronted by high misorientation between α lamellae. Furthermore, it is evidence that the crack crossing highly aligned α lamellae does so at a 90° angle to the lamellar boundaries. This observation is not surprising because the crack propagates through low-angle boundaries more easily due to reduced levels of strain and stress incompatibility. In addition, slip is easy across the α/β interface for one ⟨a⟩ direction within colonies according to the Burgers relationship. Therefore, highly aligned α lamellae will hinder crack propagation only to a very limited extent and not affect crack growth direction, whilst high misorientations between α lamellae will result in elastic and plastic incompatibility between the lamellae, thus promoting crack undulation and diversion as reported in Refs. [35–37].

A small representative section of the EBSD map recorded at 10 μm below the original surface of the sample is plotted in Fig. 13 as IPF α map (a), IPF β map (b), secondary electron image (c) and Schmid factor maps (d–g). For Fig. 13a schematic 3D hexagons have been added to some lamellae/colonies along the crack path for better visualization of the crystallographic orientation of these critical α lamellae. Close inspection of Fig. 13a shows that the crack has grown in a translamellar fashion in most cases and that in such cases the normal of the basal plane is close to a 90° angle to the crack. It should be noted that the IPF β map and secondary electron image are included in Fig. 13 in order to avoid confusion between the two types of crack undulations, where the large crack diversion and bifurcation is related to the first-order undulation as can be seen in Fig. 13b and c and discussed in Section 3.2. Fig. 13d–g represents Schmid factor maps for the most common ⟨a⟩ slip and ⟨c + a⟩ slip modes with the stress axis in the horizontal direction of the images. It is noticeable from these Schmid factor maps that the crack easily crossed the lamellae favourably oriented for ⟨a⟩ basal slip, while lamellae with a high Schmid factor for ⟨a⟩ prismatic slip and pyramidal ⟨c + a⟩ slip tended to deviate the crack. In the present study, statistical Schmid factor analysis of the EBSD maps showed that about 25% of the crack length showing translamellar crack growth had grains favourably orientated for prismatic slip, while 75% were more likely to undergo basal slip. This is certainly a surprising finding as both slip modes are usually reported to have a very similar critical resolved shear stress (CRSS) [4]. However, this might be related to the stress state at the microstructural scale [38], whereas only uniaxial loading is considered for calculating the Schmid factor in this study.

In summary, the second-order undulation of the crack seems to be largely governed by the crystallographic orientation of lamellae and lamellar colonies. Highly aligned α colonies, when preferentially orientated for basal ⟨a⟩ slip, tend to be easily crossed by a crack with the crack direction 90° to the lamellae boundaries. In contrast, large misorientations between α lamellae and lamellae preferably orientated for prismatic ⟨a⟩ slip and pyramidal ⟨c + a⟩ tend to deflect the crack direction, resulting in the second-order crack undulation observed by EBSD.

## 4. Conclusions

In the present study powder-processed Ti-6246 heat treated to have a relatively coarse lamellar microstructure has been studied during in situ fatigue loading using X-ray microtomography on beam line ID19 at the ESRF. The tomography data provided a chronological description of the crack propagation in three dimensions and enabled the identification of prior β grain boundaries. In addition, EBSD studies have been carried out on the fatigued sample, confirming the role of prior β grain boundaries and identifying the importance of the morphology and crystallographic orientation of the α lamellae.

The main findings of this work can be summarized as follows:

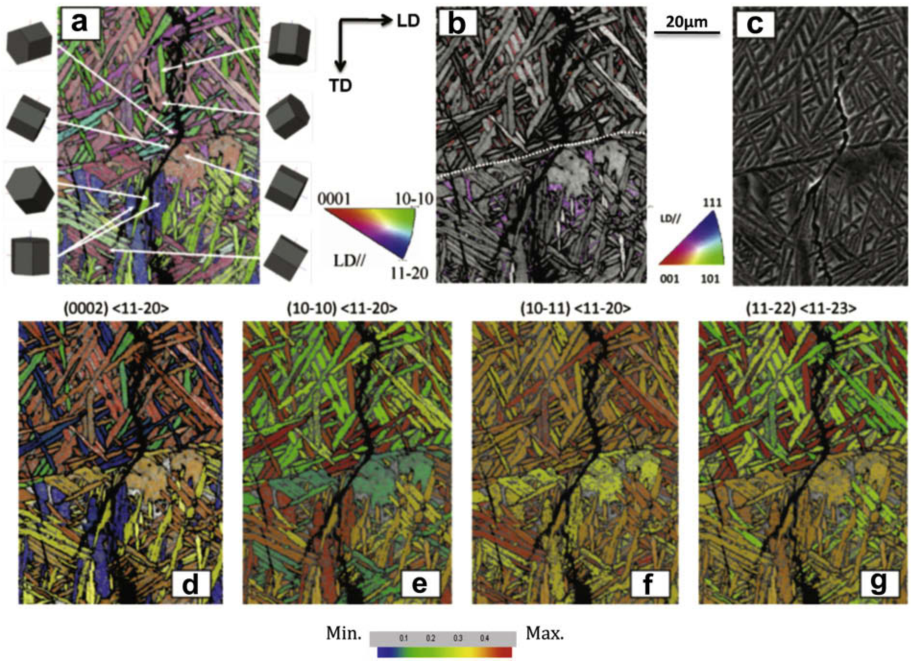

Fig. 13. EBSD-derived IPF map for α in (a) and for β in (b) showing effects of grain orientation on the crack propagation direction (3D crystal viewer superimposed on the map in (a)). (c) SEM image. (d–g) EBSD-derived Schmid factor maps for the same area in (a)–(c), the calculation carried out assuming the basal, prismatic and second-order pyramidal slip is activated as in (d), (e), (f) and (g), respectively.

- During the fatigue experiment the *a*/*c* ratio of the observed fatigue crack increased from 0.4 (initial notch) to 1.2, indicating a tendency for the crack to grow faster in the bulk than at the surface.
- 3D analysis of the stress intensity factor along the crack front could not explain the evolution of the measured *a*/*c* ratio.
- Near the surface region, crack bifurcation was found to be a dominant feature affecting the overall crack shape. The initiation of crack bifurcation could be related to the crack crossing a prior β grain boundary and more specifically β grain triple points. When the crack enters a new β grain with a different crystallographic orientation, the crack is diverted. This crack usually arrests quickly and a secondary crack forms, leading to crack bifurcation. This secondary crack growths approximately in mode I and develops into the new primary crack. During the early stage of bifurcation the crack propagates very slowly and only accelerates once the bifurcation has become a less dominant feature. Consequently, prior β grain boundaries seem to promote crack bifurcation and crack retardation near the surface, resulting in a first-order crack front undulation.
- No crack bifurcation was found deep inside the material in the presence of high constraint. Consequently the crack could grow relatively deep as observed by the evolution of the *a*/*c* ratio.
- In addition to the first-order crack shape undulation, a second-order undulation was observed by X-ray tomography and in the scanning electron microscope, which is closely related to the morphology and crystallographic orientation of the α lamellae. Translamellar crack growth was a dominant feature, but the microstructure played an important role in affecting the growth direction. EBSD studies suggest that α lamellae orientated favourably for basal ⟨a⟩ slip provided the easiest path for translamellar crack propagation.
- The crack was often found to divert when large misorientations were observed between lamellae. In addition, lamellae unfavourably oriented for basal ⟨a⟩ slip and favourably oriented for prismatic ⟨a⟩ and pyramidal ⟨c + a⟩ slip tended to deflect or possibly even arrest the crack. Although crack diversion might be expected from lamellae preferably orientated for the difficult to activate ⟨c + a⟩ slip, it is rather surprising that lamellae preferably orientated for prismatic slip ⟨a⟩ act as a barrier.

## Acknowledgements

The authors thank Dr. David Rugg from Rolls-Royce plc for financial support and material supply as well as the EPSRC for supporting this Project (EP/E048455/1). We are particularly grateful for the experimental support provided by Dr. Greg Johnson who was our local contact during the experiment on beam line ID19 at the ESRF.

## References

[1] Bhattachayya D, Viswanathan GB, Denkenberger R, Furrer D, Fraser HL. Acta Mater 2003;51:4679.
[2] Donachie MJ. Titanium: a technical guide. 2nd ed. Materials Park, OH: ASM International, The Materials Information Society; 2000.
[3] Lutjering G. Mater Sci Eng 1998;A243:32.
[4] Lutjering G, Williams JC. Titanium: engineering materials and processes. 2nd ed. Heidelberg: Springer Verlag; 2007.
[5] Schroeder G, Albrecht J, Luetjering G. Mater Sci Eng 2001;A319–321:602.
[6] Hu YM, Floer W, Krupp U, Christ HJ. Mater Sci Eng 1999;A278:170.
[7] Bin L, Yong L, Xiao-yu H, Hui-ping T, Li-fang C. Trans Nonferr Metal Soc China 2008;18:227.
[8] Sarrazin-Baudoux C. Int J Fatigue 2005;27:773.
[9] Sarrazin C, Chiron R, Lesterlin S, Petit J. Fatigue Fract Eng Mater Struct 1994;17(12):1383.
[10] Bantounas I, Lindley TC, Rugg D, Dye D. Acta Mater 2007;55:5655.
[11] Hurley PJ, Whittaker MT, Williams SJ, Evans WJ. Int J Fatigue 2008;30:623.
[12] Benedetti M, Fontanari V, Lutjering G, Albrecht J. Eng Fract Mech 2008;75:169.
[13] Cox BN. Eng Fract Mech 1989;33(4):655.
[14] Ravichandran KS. Fatigue Fract Eng Mater Struct 1997;20(10):1423.
[15] Khor KH, Buffiere JY, Ludwig W, Sinclair I. Scripta Mater 2006;55:47.
[16] Sadananda K, Vasudevan AK. Int J Fatigue 2005;27:1255.
[17] Ludwig W, Buffière JY, Savelli S, Cloetens P. Acta Mater 2003; 51(3):585.
[18] Karadge M, Babout L, Garcia-Pastor F, Ludwig W, Withers PJ, Buffiere J-Y, Preuss M. In: Proceedings of the 11th world conference on titanium (Ti 2007), Kyoto. Sendai: The Japan Institute of Metals; 2007. p. 239.
[19] Cloetens P, Pateyron-Salome M, Buffière JY, Peix G, Baruchel J, Peyrin F, Schlenker M. J Appl Phys 1997;81(9):5878.
[20] Bache MR, Germain L, Jackson T, Walker ARM. In: Proceedings of the 11th world conference on titanium (Ti 2007), Kyoto. Sendai: The Japan Institute of Metals; 2007. p. 523.
[21] Buffiere JY, Ferrie E, Proudhon H, Ludwig W. Mater Sci Technol 2006;22(9):1019.
[22] Newman JC, Raju IS. Eng Fract Mech 1981;15(1–2):185.
[23] Cox BN, Morries WL. Eng Fract Mech 1988;31(4):591.
[24] Ferrie E, Buffiere JY, Ludwig W, Gravoil A, Edwards L. Acta Mater 2006;54:1111.
[25] Newman Jr JC, Raju IS. Fracture mechanics. In: Lewis JC, Sines G, editors. Proceedings of the 14th symposium, Los Angeles, CA. Theory and analysis, vol. 1. West Conshohocken, PA: ASTM; 1983. p. 238.
[26] Bache MR, Evans WJ, Suddel B, Herrouin FRM. Int J Fatigue 2001;23:153.
[27] Bache MR, Evans WJ. Mater Sci Eng 2001;A319–321:409.
[28] Wojcik CC, Chan KS, Koss DA. Acta Mater 1998;36(5):1261.
[29] Bache MR, Evans WJ, Randle V, Wilson RJ. Mater Sci Eng 1998;A257:139.
[30] Toda H, Sinclair I, Buffiere JY, Maire E, Khor KH, Gregson P, et al. Acta Mater 2004;52:1303.
[31] Kim WH, Laird C. Acta Mater 1978;26:777.
[32] Gourgues AF. Mater Sci Technol 2002;18:119.
[33] Birosca S, Dingley D, Higginson RL. J Microsc 2004;213(3):135.
[34] Dieter GE. Mechanical metallurgy. Singapore: McGraw-Hill; 1998.
[35] Tanaka K, Mura T. Mech Mater 1981;1:63.
[36] Wright SI, Field DP. Mater Sci Eng 1998;A257:165.
[37] Huang ZW, Bowen P, Davey S, Blenkinsop PA. Scripta Mater 1998;38(7):1117.
[38] Bridier F, Villechaise P, Mendez J. Acta Mater 2005;53:555.